



Kent Academic Repository

Symington, Adam R., Molinari, Marco, Moxon, Samuel, Flitcroft, Joseph M., Sayle, Dean C. and Parker, Stephen C. (2020) *Strongly Bound Surface Water Affects the Shape Evolution of Cerium Oxide Nanoparticles*. *The Journal of Physical Chemistry C*, 124 (6). pp. 3577-3588. ISSN 1932-7447.

Downloaded from

<https://kar.kent.ac.uk/80395/> The University of Kent's Academic Repository KAR

The version of record is available from

<https://doi.org/10.1021/acs.jpcc.9b09046>

This document version

Author's Accepted Manuscript

DOI for this version

Licence for this version

UNSPECIFIED

Additional information

Versions of research works

Versions of Record

If this version is the version of record, it is the same as the published version available on the publisher's web site. Cite as the published version.

Author Accepted Manuscripts

If this document is identified as the Author Accepted Manuscript it is the version after peer review but before type setting, copy editing or publisher branding. Cite as Surname, Initial. (Year) 'Title of article'. To be published in *Title of Journal*, Volume and issue numbers [peer-reviewed accepted version]. Available at: DOI or URL (Accessed: date).

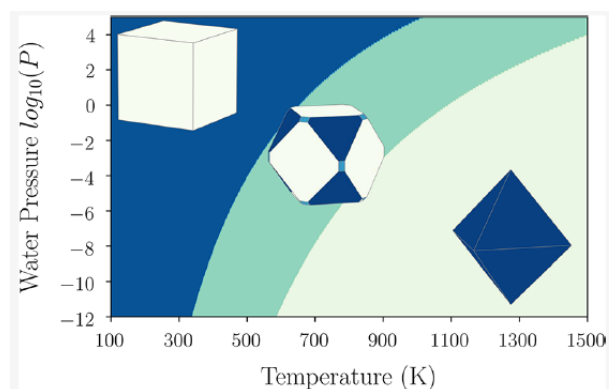
Enquiries

If you have questions about this document contact ResearchSupport@kent.ac.uk. Please include the URL of the record in KAR. If you believe that your, or a third party's rights have been compromised through this document please see our [Take Down policy](https://www.kent.ac.uk/guides/kar-the-kent-academic-repository#policies) (available from <https://www.kent.ac.uk/guides/kar-the-kent-academic-repository#policies>).

Strongly Bound Surface Water Affects the Shape Evolution of Cerium Oxide Nanoparticles

Adam R. Symington, Marco Molinari, Samuel Moxon, Joseph M. Flitcroft, Dean C. Sayle, and Stephen C. Parker

ABSTRACT: The surface structure and composition of functional materials are well-known to be critically important factors controlling the surface reactivity. However, when doped the surface composition will change, and the challenge is to identify its impact on important surface processes and nanoparticle morphologies. We have begun to address this by using a combination of density functional theory and potential-based methods to investigate the effect of surface dopants on water adsorption and morphology of the technologically important material, CeO₂, which finds application as electrolyte in SOFCs, catalyst in soot combustion, and enzyme mimetic agents in biomedicine. We show that by mapping CeO₂ surface phase diagrams we can predict nanoparticle morphologies as a function of dopant, temperature, and water partial pressure. Our results show that low-temperature, undoped CeO₂ nanocubes with active {100} surface sites are thermodynamically stable, but at the typical high temperature, operating conditions favor polyhedra where {100} surfaces are replaced by less active {111} surfaces by surface ion migration. However, doping with trivalent cations, such as Gd³⁺, will increase binding of water on the {100} surfaces and hence act to preserve the cuboidal architecture by capping the active surfaces. As surfaces tend to be decorated by impurities and dopants it is clear that their role should receive more attention and the approach we describe can be routinely applied to nanomaterials, morphologies, and associated active/inactive surfaces.



Introduction

The control of nanoparticle growth and evolution is an important topic that is tackled experimentally using SEM and TEM in the presence of biological macromolecules,¹ organic molecules,² and polymers.³ This is not limited to the presence of molecules in the surrounding environment but also to nanoparticles' response to external variables such as the high energy electron beam of a TEM.⁴ There has been recent work on defining rules to determine the evolution of nanoparticle shape;⁵ however, the challenge is also to correlate the shape of nanoparticles to external variables such as pressure and temperature. We present a comprehensive way to predict nanoparticle shape as a function of water partial pressure and temperature in both stoichiometric and doped nanoparticles. We demonstrate this methodology by applying it to CeO₂ as it is an important catalyst, prevalent in a wide range of processes, and because the relationship between shape and the surrounding environment remains largely unexplored.

Cerium oxide, CeO₂ (Ceria), and doped derivatives are important technological materials. Thanks to the easily accessible redox conversion between Ce³⁺ and Ce⁴⁺ and the oxygen vacancy tolerance of the fluorite structure, ceria enjoys a wide spectrum of applications like electrochemical sensors,^{6,7} solid oxide fuel cells (SOFCs),⁸⁻¹¹ catalytic exhaust treatment,¹² hydrogen fuel generation,¹³ and biomedicine.^{14,15} For each of its many applications, the redox capability is essential to the performance of the materials.

As the redox reactions take place at the materials surfaces, the understanding of surface morphology and chemistry is key to the design and engineering of ceria-based materials. Despite its presence in many chemical reactions as either a solvent, spectator, or reagent, water and its effect on the morphology of ceria nanoparticles is often overlooked. Most investigations focus on the oxygen reduction and incorporation at the electrolyte-cathode-gas triple-phase boundary in SOFCs and neglect the contribution from water vapor in the gaseous atmosphere being fed at the cathode of the SOFC. Experiments have shown that water does have a significant impact on the oxygen-transport properties of both pure and doped ceria at relevant operating temperatures.^{16,17} However, the details behind these changes are largely unclear.¹⁸ Thus, it is important to know at what temperature water will still be present at the surfaces of doped ceria. While surface water is undesirable in soot oxidation and SOFCs, other catalytic processes depend on water dissociation at the surface, e.g., the water gas shift reaction. Another important question considered is the role that particle morphology has on catalytic performance; what is less well-known is how the morphology of the material affects and is affected by the interaction with water, especially if the material is in use over a long period of time, i.e., over many catalytic cycles. Significant theoretical effort has been made to predict how water adsorbs at both stoichiometric and reduced ceria surfaces.¹⁹⁻²² However, in technological applications ceria is doped, and the interplay between water and doped ceria surfaces has not yet been fully explored. Clearly, given the technological importance and the wide range of uses of doped ceria, the effect of water adsorption warrants further study.

In this work, we describe our study of the interaction of water with the most important low index surfaces of CeO₂ ({111}, {110}, and {100}) when doped with Y³⁺, Sm³⁺ and Gd³⁺ cations. The latter is particularly important in SOFC applications. Thus, we aim to evaluate whether these trivalent cations strongly segregate to these surfaces and predict their effect on the equilibrium morphology and water adsorption. Thus, we demonstrate the extent to which morphology is linked to surface composition and hence comment on the relationship between catalytic activity and nanoparticle shape evolution.

Methodology

Calculation Details. Density functional theory (DFT) calculations were performed using the Vienna Ab-initio Simulation Package (VASP) code,^{23,24} within which projector augmented-wave pseudopotentials and a plane wave cutoff of 500 eV were used. A Γ -centered K-point grid of $2 \times 2 \times 1$ with the third vector perpendicular to the surface plane was used. Both the cutoff and K-points were tested for convergence. Calculations were carried out using the generalized gradient approximation (GGA) exchange-correlation functional of Perdew (PBE), with the + U correction of Dudarev²⁵ to account for on-site Coulombic interactions. A U value of 5 eV is applied to Ce f states.^{14,19} The structures were optimized until the residual forces on each atom were less than 10 meV Å⁻¹. All calculations were spin polarized and an initial ferromagnetic ordering was used throughout, which has been shown to produce no difference in the energetics of CeO₂ systems.^{26,27} Dispersion corrected methods were tested but did not provide significant improvements to the accuracy of the results and have thus not been employed further. Isolated O₂ and H₂O molecules were simulated using a 10 Å³ cubic cell. The K point density and the same convergence criteria as the surface calculations were also used for these molecules.

Surface Energies and Thermodynamic Framework. The physical quantity defining stable surface compositions is the surface energy γ (J m⁻²). Using the slab method, which uses a simulation cell with two symmetric surfaces, the surface energy of a stoichiometric slab (γ_{stoich}) can be calculated from the energy of the systems containing the slab ($E_{\text{stoich,bare}}$), the energy of ceria stoichiometric bulk ($E_{\text{bulk,CeO}_2}$), and the surface area (S)

$$\gamma_{\text{stoich}} = \frac{E_{\text{stoich,bare}} - E_{\text{bulk,CeO}_2}}{2S} \quad (1)$$

The surface energy of the doped surfaces (γ_{doped}) was calculated according to

$$\gamma_{\text{doped}} = \frac{E_{\text{slab,M}_2\text{O}_3} - (E_{\text{bulk,CeO}_2} + E_{\text{bulk,M}_2\text{O}_3})}{2S} \quad (2)$$

where $E_{\text{slab,M}_2\text{O}_3}$ is the energy of the doped slab and $E_{\text{bulk,M}_2\text{O}_3}$ is the energy of the bulk dopant.

The heat of reduction was calculated for the three low index surfaces of ceria by creating an oxygen vacancy through the removal of a surface oxygen atom. Two electrons are left behind and localize on the cerium ions neighboring the vacancy.

Literature studies have suggested oxygen vacancies are stable in the surface layer,²⁸⁻³⁰ but there is debate with others suggesting that vacancies prefer to exist in the subsurface.³¹⁻³³ We have assumed that the water will interact most strongly when the oxygen vacancies are located at the surface and that the vacancy and adsorbent are near the Ce(III) and dopants. We do recognize that different distributions of 3+ and V_o are accessible^{34,35} and that the dissociation of water at the surface is aided by surface vacancies,^{36,37} which may cause small differences in energies. For example, Aparicio-Angleset al. have shown that V_o "can be placed fairly randomly in the surface" of CeO₂ {111} as there are very similar energetics between the different configurations; however, the V_o is more stable if situated in the second oxygen layer.³⁵ However, we have shown previously, that at operating conditions, oxygen vacancies will be mobile and hence consider that the sites we have chosen are representative, easily reproducible and consistent with earlier studies.³⁸ Furthermore, to demonstrate the presence of surface oxygen vacancies within the context of our models we have carried out large scale molecular dynamics simulations of cerium oxide surfaces containing oxygen vacancies and observed that vacancies occupy both the surface and subsurface layers. Full details are included in the [Supporting Information](#).

The heat of reduction is calculated according to

$$E_{\text{reduction}} = \frac{(E_{\text{slab,reduced}} + E_{\text{O}_2}) - E_{\text{stoich,bare}}}{2} \quad (3)$$

$E_{\text{reduction}}$ is the reduction energy, $E_{\text{slab,reduced}}$ is the DFT energy of the surface containing an oxygen vacancy, and E_{O_2} is the DFT energy of oxygen. [Equations 1 and 2](#) provide surface energies neglecting temperature and hence are not representative for the operating conditions of various catalytic processes and the synthesis and sintering conditions. For the hydrated surfaces, the effect of temperature is introduced as follows^{19,39,40}

$$\gamma_{\text{adsorbed,T,P}} = \gamma_{\text{bare}} + \left(C \left(E_{\text{ads,T}} - RT \ln \left(\frac{p_{\text{H}_2\text{O}}}{p^\circ} \right) \right) \right) \quad (4)$$

where C is the coverage of water, γ_{bare} is the surface energy of the base surface, and γ_{stoich} could be calculated according to [eq 1](#) for the stoichiometric surfaces or γ_{doped} from [eq 2](#) for the reduced and doped surfaces. The average adsorption energy of all water ($E_{\text{ads,T}}$) in each configuration was calculated according to

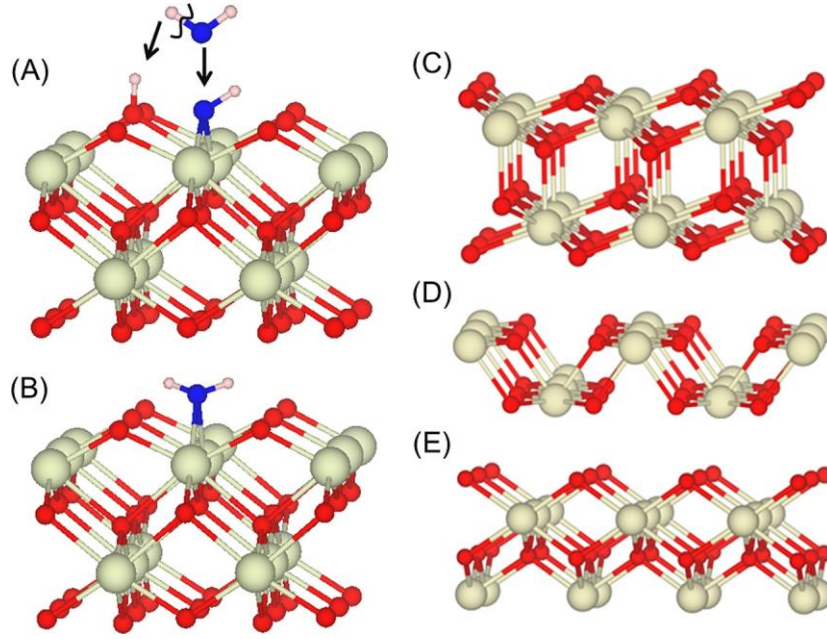


Figure 1. Schematic representation of dissociative (A) and molecular (molecular) (B) adsorption of water on the {100} surface. Side view of the {111} (C), {110} (D), and {100} (E) surfaces. Cerium ions are shown in cream, surface oxygen ions in red, water oxygen ions are shown in blue and hydrogen ions are shown in white.

$$E_{\text{ads},T} = E_{\text{Hyd}} - (E_{\text{slab,bare}} + n_{\text{H}_2\text{O}} E_{\text{H}_2\text{O},(T)}) / n_{\text{H}_2\text{O}} \quad (5)$$

where E_{Hyd} is the energy of the slab with the adsorbed species, E_{bare} is the energy of the bare surface, and $n_{\text{H}_2\text{O}}$ is the number of adsorbed H_2O molecules. The temperature-corrected water energy was calculated according to

$$E_{\text{H}_2\text{O},(T)} = E_{\text{H}_2\text{O},(\text{oK,g})} - TS(T) \quad (6)$$

where $S(T)$ is the experimental entropy of gaseous water in the standard state.

On the basis of the surface energies calculated according to eq 4, the surface area of each surface was calculated using the Wulff construction.⁴¹⁻⁴³ These areas were then combined to give the ratio between each surface under varying pressure and temperature.

Surface Models. The structure of stoichiometric bulk CeO_2 retains the fluorite crystal structure (space group $Fm\bar{3}m$) despite a small expansion of the unit cell. This is a well-documented effect for the DFT methodology employed in this study.²⁶ The simulated lattice parameter ($a = 0.545$ nm) compares well with the experimental lattice parameter of ($a = 0.541$ nm). Model structures were generated using the METADISE code.⁴² 3D boundary conditions were used throughout, and hence, the surfaces were modeled using the slab method⁴⁴ in which a finite number of crystal layers is used to generate two identical surfaces via the introduction of a vacuum gap perpendicular to the surface. A vacuum gap of 15 Å was used to minimize the interaction between images. All slab calculations use symmetric introduction of, adsorbates, oxygen vacancies and dopants to both sides of the slab, thus ensuring that the surfaces were identical and the cell had no net dipole moment.

The {100} and {110} slabs with a $p(2 \times 2)$ expansion of the surface unit cell included 13 and 7 atomic layers (24 and 28 CeO_2 units, respectively), while the {111} slab with a $p(2 \times 3)$ expansion included 12 atomic layers (24 CeO_2 units).

We have considered water adsorption on the stoichiometric surface of ceria, referred to as Ce(IV) surfaces, reduced surfaces, where an oxygen vacancy has been introduced to the surface, referred to as Ce(III) and doped surfaces, referred to as M^{3+} , where M is Sm, Gd, and Y.

In this work, the amount of water in each calculation is expressed in terms of coverage, which is the number of water molecules per square nanometer. We have investigated different water coverages on each surface up to a monolayer coverage on each surface, which corresponds to one water molecule per surface CeO_2 unit. As the number of configurations for adsorbed water on surfaces of ceria is extremely large, we have limited the choice to structures that have previously been suggested and that maximize the coordination between the adsorbate and the surface.^{19,45} Several configurations for the lowest water coverage were then computed, but only the most stable one is reported. M^{3+} atoms were distributed according to the defect ordering of the system. For all systems, only the most stable water configuration has been reported.

Phase diagrams were generated, and analysis was conducted using the surfinpy code.⁴⁶ Wulff constructions were generated using pymatgen,⁴⁷ and all figures were drawn using VESTA.⁴⁸

Molecular Dynamics. To simulate the kinetics of the cube-to-polyhedron morphological change a model nanocube, generated previously was used.⁴⁹ The model comprises 6921 CeO_2 repeat units and exposes six {100} surfaces. Molecular dynamics (MD) simulations, using the DLPOLY code,⁵⁰ were then performed at 5100 K for 200 ns using an NVT ensemble. This enabled any energy associated with, for example a cube-to-polyhedron shape change, to be extracted via a thermostat. If it were not extracted, the heat energy would melt the nanoparticle. This methodology has been used successfully in previous studies in order to study nanoparticle transformations at a reasonable computational cost.⁵¹⁻⁵⁵

The Born model of the ionic solid was used to represent the interactions between the Ce and O ions comprising the

nanoparticle using potential parameters derived by Minervini et al.⁵⁶ A rigid ion model representation was used to reduce computational cost. Molecular graphics, using the VMD code,⁵⁷ were used extensively to track the change in morphology with time and elucidate the atom-transport mechanism (Figure 1).

Results

Surface Energy. The calculated surface energies obtained from eq 1 are 1.44, 1.06, and 0.71 J/m² for the {100}, {110}, and {111} surfaces, respectively, which agrees with previously calculated surface energies (1.4, 1.0, and 0.7 J/m²,²⁶ 1.41, 1.04, and 0.69 J/m²,⁵⁸). The heat of reduction associated with the three surfaces, which corresponds to the ease to remove surface oxygen ions, follows the order {111} > {100} > {110} with values of 1.96, 1.54, and 1.20 eV, respectively, which agree with those reported in the literature.^{28–30}

We have calculated the surface energy of the M₂O₃-doped surfaces according to eq 1. The results in Figure 2 show that on

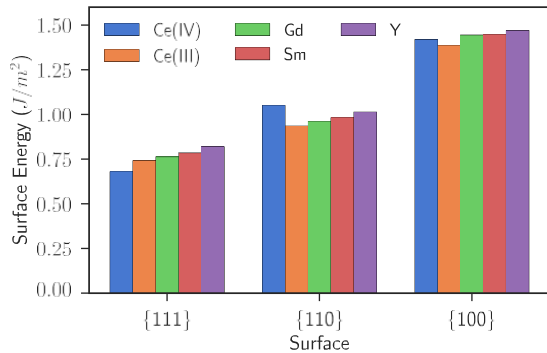


Figure 2. Surface energies for the Gd³⁺ doped, Sm³⁺ doped, and Y³⁺ doped {111}, {110}, and {100} surfaces (green, red, and purple) in comparison to the stoichiometric (Ce(IV)) and reduced (Ce(III)) surfaces (blue and orange).

reduction there is a decrease in surface energy on reduction of the {110}/{100} surfaces and an increase on the {111}. All surfaces see an increase in surface energy on addition of M₂O₃ (M = Gd, Sm and Y) dopants when compared to the reduced system. While there is an order of stability that follows Ce(III) < Gd < Sm < Y, there is only a difference of 0.02 J/m² between the lowest (Gd) and highest (Y) on each surface.

We have calculated the surface energy, namely the energy to cleave the M₂O₃ doped surfaces according to eq 2 at constant oxygen stoichiometry. The results in Figure 2 show that there is a decrease in surface energy when Ce(III) and oxygen vacancies are present compared to the stoichiometric surface. On replacing Ce(III) with other 3+ dopants we see an increase in surface energy. However, while the order of stability follows the size of dopant, Ce(III) < Gd < Sm < Y, there is only a small difference of 0.02 J/m² between the lowest (Gd) and highest (Y) on each surface. When considering the surface terminations in the fully oxidized form, i.e. no Ce(III) present, there is a more complex pattern, with the {111} surface energy increasing on doping, {110} reducing and the {100} virtually unchanged, which may have implications for adsorption.

Water Adsorption at the Lowest Coverage. The water adsorption energy is shown in Figure 3A. The adsorption energy at low water coverage is found by evaluating the energy of an isolated single water molecule at the surfaces. As

expected, the water adsorption energies on stoichiometric surfaces follow the surface energy; i.e., the least stable have a larger adsorption energy.

All M³⁺-doped and reduced (Ce(III)) surfaces have a stronger affinity for water than the corresponding stoichiometric surfaces.¹⁹ This is due to the presence of a vacancy, which binds 3+ cations at the surface, as shown in previous experimental and theoretical studies.⁵⁹ Hydroxyl groups can fill the vacant oxygen lattice site and heal the surface enabling the surface cations to recover coordination. Associatively adsorbed water cannot adequately enable this healing and thus surface oxygen vacancies promote dissociation of water molecules. We find spontaneous dissociation of water molecules in the presence of surface oxygen vacancy, implying a barrier-less process.

Dissociative adsorption is favored on the {111} surface, but water can still be adsorbed as a molecular species, in line with previous experimental⁶⁰ and computational^{19,22,61} literature. Experimental observation of dissociation of water is also found for Gd³⁺ doped CeO₂ surfaces by Perez-Coll et al.⁶² and Kossoy et al.⁶³

Comparison between M³⁺ and Ce(III) shows that dopants decrease the affinity of the {111} and {110} surfaces for water but enhance the affinity for water on the {100} surface (Figure 3A). On all surfaces there is a clear order of stability between the dopants, and this follows the order Sm³⁺ > Gd³⁺ > Y³⁺. The difference in adsorption energy is likely to arise from surface strain due to the impurity. The order of ionic radii follows Ce(III) > Sm³⁺ > Gd³⁺ > Y³⁺ with Sm³⁺ being the closest in size to Ce³⁺. The average Sm³⁺-O bond length (2.36 Å) is the longest and closest to the Ce-O bond distance (2.34 Å), whereas the average Y³⁺-O is slightly shorter (2.30 Å).

Water Coverage dependence. The water adsorption energy as a function of water coverage is shown in Figure 3B–D. The three surfaces show remarkably different behavior when the water coverage increases. The most energetically favorable adsorption at the lowest coverage is on the {100} surface followed by the {111} and finally the {110}; however, at higher coverage the order {100} > {110} > {111} is followed.

Another difference is the change of the adsorption energy with coverage for these surfaces. Adsorption on the {111} and {100} surfaces is less energetically favorable with increasing water coverage up to the monolayer adsorption (i.e., a water molecule per surface Ce). However, on the {110} surface there is an initial stabilization at 25% and 50% coverage followed by a destabilization of the adsorption when monolayer coverage is reached. This is likely due to the surface area available per surface Ce atom on the {110}, 0.21 nm² against the 0.19 and 0.15 nm² on the {111} and {100}, which can accommodate a greater coverage of water before steric effects start destabilizing further adsorption of water. It is clear that the hydrogen bonding network on the {111} and {100} surfaces can easily form as the coverage of water increases; this is not the case for the {110}, where the water molecules are adsorbed and isolated by direct interaction with surface Ce.

All surfaces stabilize dissociative adsorption at low coverage but a mixture of associatively and dissociatively adsorbed water adsorption occurs at the monolayer, again to maximize hydrogen bonding at the surface. Sm³⁺ shows the greatest strength of adsorption compared to Y³⁺ and Gd³⁺ at the lowest coverage (Figure 3), although at the monolayer coverage this relationship is lost. This suggests that the M³⁺-water

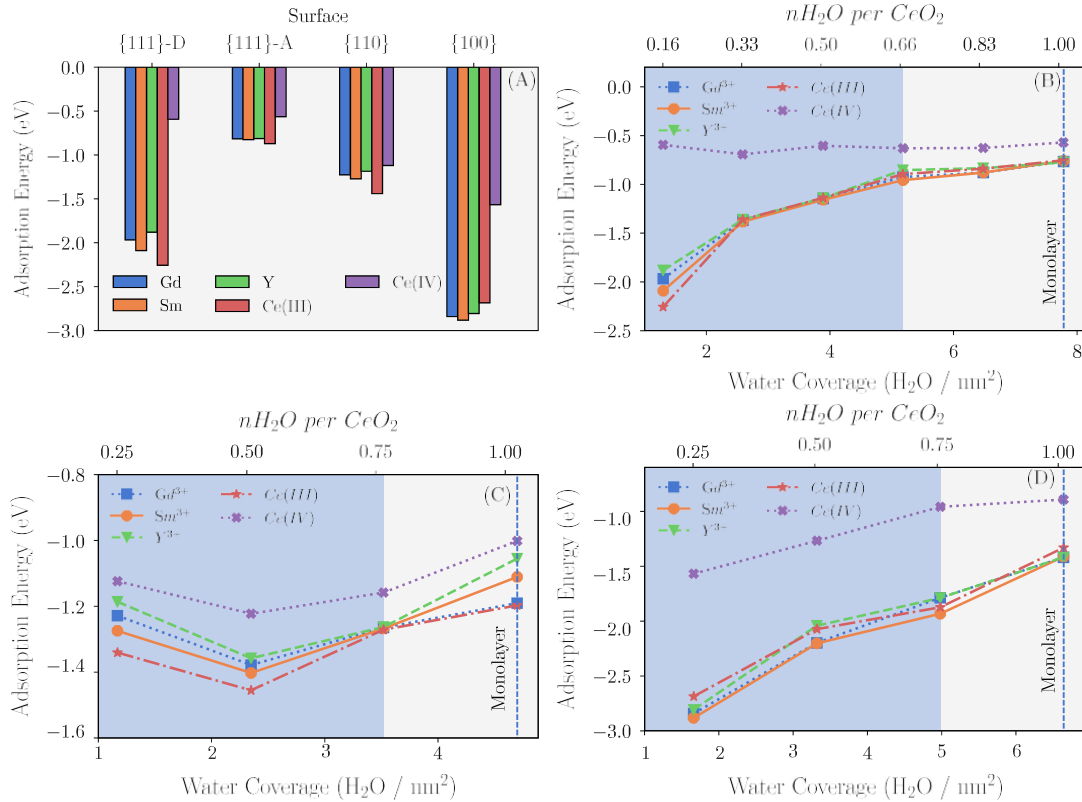


Figure 3. (A) Adsorption energies for water on the low index surfaces of ceria for a coverage of $1.66 \text{ H}_2\text{O}/\text{nm}^2$ for dissociative water on the $\{111\}$, associative water on the $\{111\}$, $1.17 \text{ H}_2\text{O}/\text{nm}^2$ for dissociative water on the $\{110\}$, and $1.30 \text{ H}_2\text{O}/\text{nm}^2$ for dissociative water on the $\{100\}$. Ce(IV), Ce(III), Sm³⁺, Gd³⁺, and Y³⁺ are denoted by red, purple, blue, orange, and green bars, respectively. As both dissociatively and associatively adsorbed water can be stabilized on the $\{111\}$ these are denoted by $\{111\}$ D and $\{111\}$ A respectively. (B–D) Adsorption energy (eV) per water as a function of coverage for (B) $\{111\}$, (C) $\{110\}$, (D) $\{100\}$; for Gd³⁺ doped (blue squares), Sm³⁺ doped (orange circles), Y³⁺ doped (green triangles), Ce(III) (red stars), and Ce(IV) (purple crosses) ceria. The shaded area corresponds to the coverage range where dissociative adsorption is favored, and the unshaded region corresponds to a coverage range where a mixture of molecular and dissociative water occurs.

interaction dominates, but at higher water coverage this is lost as the hydrogen bonding network becomes the discriminating factor defining surface stabilization.

Our data indicates that dopants have very little impact on the water adsorption on the $\{111\}$ surface at all coverages. The largest difference in water adsorption energies is at the lowest coverage of $1.30 \text{ H}_2\text{O}/\text{nm}^2$ (0.4 eV); at higher coverages there is only a minimal difference between the impurity covered and reduced surfaces. On the $\{100\}$ surface, there is a modest difference (up to 0.1 eV) in adsorption energy at all coverages. The greatest impact is found for the $\{110\}$ surface, with the exception of $3.5 \text{ H}_2\text{O}/\text{nm}^2$, which marks the change in water behavior (from dissociative to a mixture of dissociative/associative) where there is virtually no difference between the strength of adsorption of water depending on the nature of the dopant, all other coverages see a marked influence: Ce(III) is always the cation that stabilized the adsorption the most and Y³⁺ the least.

Our data supports the findings of Mullins et al., who performed XRD analysis on stoichiometric $\{111\}$ and $\{100\}$ surfaces and concluded that both associatively and dissociatively adsorbed water is present at the surface.⁶⁰ They also conclude that dissociatively adsorbed water is considerably more stable on the $\{100\}$ than the $\{111\}$. There are no data available on the $\{110\}$; however, our data suggest that this is also the case for the $\{110\}$ (Figure 3D).

Phase Diagrams. We evaluated the relative stability of the three low index surfaces as a function of temperature and partial pressure of water (eq 4). This has been successfully implemented in other work^{39,40,45} as well as on CeO₂¹⁹ (later verified experimentally⁶⁰) and more recently on fluorite-structured UO₂.⁴⁵ Parts A and B of Figure 4 show the pressures as a function of desorption temperatures for the stoichiometric and reduced/doped surfaces calculated according to eq 4. Full temperature vs pressure surface phase diagrams for each data set can be found in the [Supporting Information](#).

Generally, the dopants moderate the interaction with water depending on the surface. In the case of the $\{111\}$ and $\{110\}$ surfaces, dopants reduce the surface stability of water at the surface, and thus, the surface will lose water at lower temperatures. In contrast, on the $\{100\}$ surface, the dopants stabilize adsorbed water. The introduction of oxygen vacancies (alongside the dopants Ce(III), Sm³⁺, Gd³⁺, Y³⁺) greatly increases the temperature range that water is adsorbed on the surface. This is due to a “healing” effect that occurs whereby water, in the form of hydroxyl groups, persists at the surface, at the vacant oxygen sites. This is illustrated in Figure 4C,D, where at low temperatures (blue region) the surfaces are fully covered by a monolayer of water, whereas at higher temperatures (white region) the bare stoichiometric surface is more stable. When M₂O₃ doping occurs, at intermediate temperatures, the healed region (green) is the pressures and

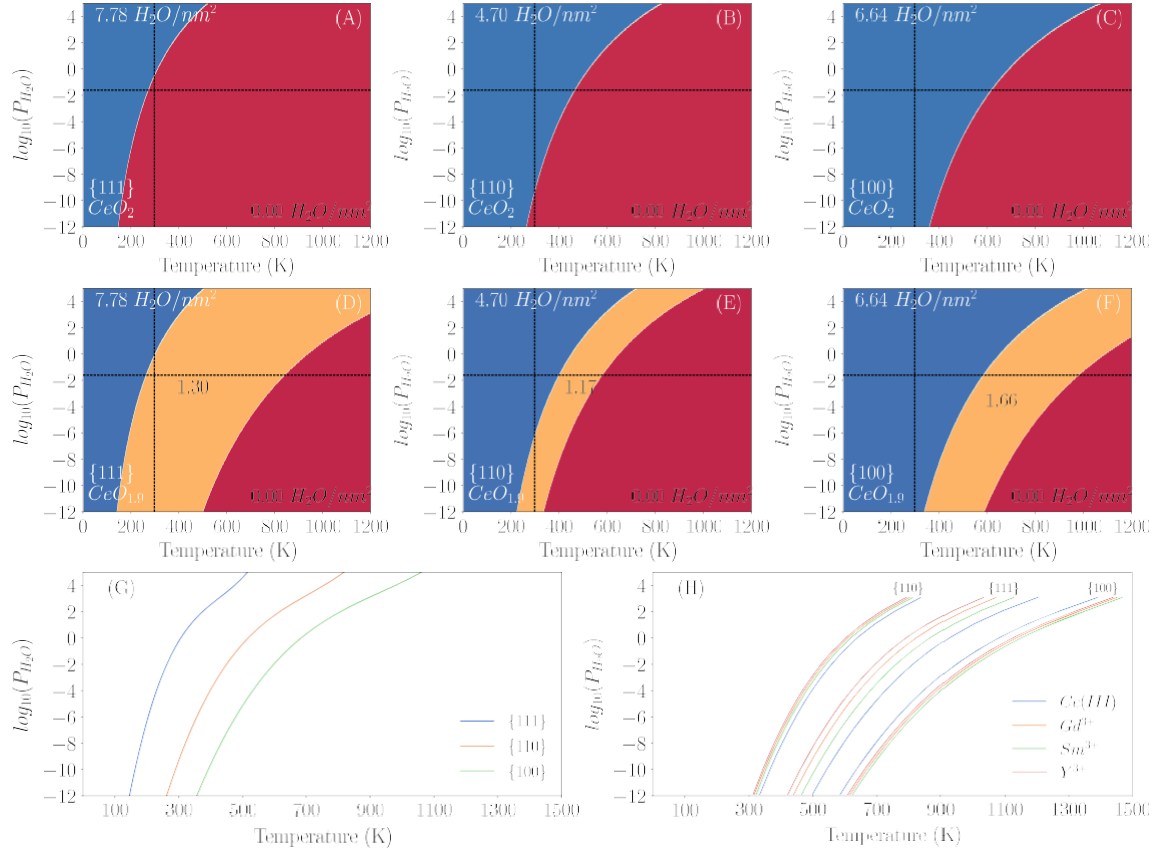


Figure 4. Phase boundary between dry (stoichiometric) and wet (surfaces with at least one water molecule) surfaces as a function of water partial pressure and temperature. Phase diagrams for water on the stoichiometric {100} (A) {110} (B), {111} (C) surfaces and reduced {100} (D) {110} (E), {111} (F) surfaces. The water coverage within each region has been labeled for clarity. (G) Water desorption temperatures at different partial pressures of water on stoichiometric {111} (blue), {110} (orange), and {100} (green) surfaces (CeIV), (H) desorption temperatures for water on the reduced (Ce(III)), Gd³⁺, Sm³⁺, and Y³⁺ surfaces (blue, orange, green, and red lines) surfaces.

Table 1. Water Desorption Temperature of Stoichiometric, Reduced, and Doped Surfaces of CeO₂ at Different Water Partial Pressures from Typical Ultrahigh Vacuum Conditions to 100% Humidity

	desorption temperature K								
	pressure = 10 ⁻¹² bar			pressure = 10 ⁻¹⁰ bar			pressure = 0.025 bar		
	{111}	{110}	{100}	{111}	{110}	{100}	{111}	{110}	{100}
Ce(IV)	154	275	382	172	304	420	270	462	613
Ce(III)	521	349	610	571	384	667	837	575	975
Gd ³⁺	460	332	643	505	367	702	744	549	1025
Sm ³⁺	486	338	651	533	372	711	783	557	1038
Y ³⁺	441	328	636	485	362	694	715	542	1014

temperatures where the dissociative water heals and stabilizes the surface. This observation is supported by Chen et al., who proposed that the first layer of water on the {111} reduced surface adsorbs dissociatively and fills the oxygen vacancies,⁶⁴ and Kossov who proposed that oxygen vacancy sites are the first to be occupied on Gd-doped ceria {111} surfaces.⁶³

Desorption Temperature. The temperature of desorption can be evaluated from the pressure-temperature phase diagrams. Our calculated desorption temperatures are in good agreement with those calculated by Molinari et al. for the stoichiometric surfaces and show reasonable agreement with the reduced surfaces, although it should be noted that we examined a range of coverages whereas only a single coverage was considered previously.¹⁹ Our work is also in agreement with other experimental work.^{22,60} Desorption temperatures

have not been previously calculated for M₂O₃-doped ceria surfaces. Desorption temperatures for each surface across a range of temperatures are shown in Table 1.

The difference between the desorption temperature of the M³⁺ doped and stoichiometric surfaces is shown in Figure 5A, and the difference between the desorption temperature on the reduced surfaces and doped surfaces is shown in Figure 5B. These were calculated as $T_{M^{3+},slab} - T_{stoich,slab}$ and $T_{doped,slab} - T_{reduced,slab}$, respectively.

Introducing dopants and reduction of the surface (controlling oxygen partial pressure) are two ways of modifying the oxygen stoichiometry of the surface. In our models, the reduced and doped surface have an equal concentration of oxygen vacancies, thus the variable at the surface is the cation, e.g., Gd³⁺ vs Ce³⁺. We find when comparing with the

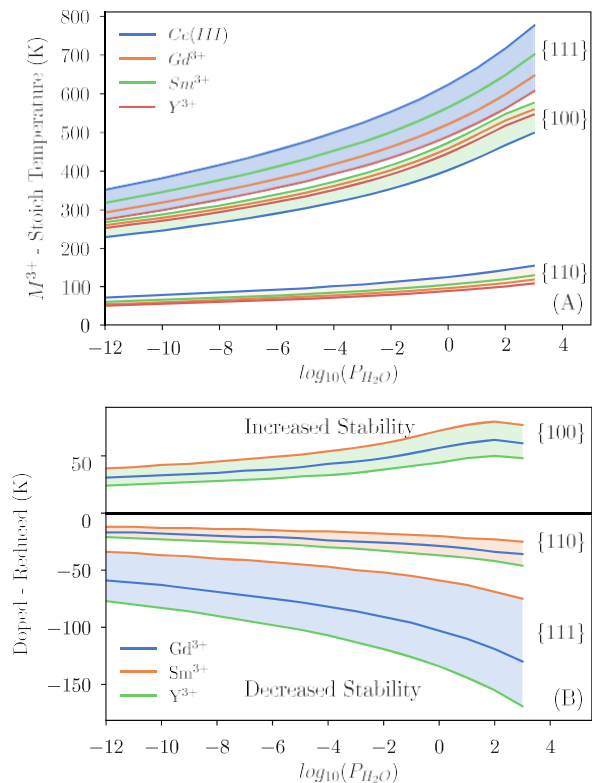


Figure 5. (A) Difference in desorption temperatures for doped surfaces compared to stoichiometric surfaces, calculated as $T_{M^{\text{doped}}^{\text{slab}}} - T_{\text{stoich}^{\text{slab}}}$. The reduced (Ce(III)), Gd^{3+} -doped, Sm^{3+} -doped, and Y^{3+} -doped surfaces are shown in blue, orange, green, and red, respectively. (B) Difference in desorption temperature between doped surfaces and reduced surfaces, calculated as $T_{\text{doped}^{\text{slab}}} - T_{\text{reduced}^{\text{slab}}}$. Gd^{3+} , Sm^{3+} , and Y^{3+} are denoted by the blue, orange, and green lines. The blue, orange, and green shaded areas correspond to the {111}, {110}, and {100} data sets.

stoichiometric surfaces (Figure 5A) that doping or reducing increases the temperature where water is stable, although for the {110} surface this is less marked. In contrast, when comparing the doped surfaces with the reduced surfaces we predict that dopants on the {111} and {110} surfaces reduce the temperature of desorption for water while only the {100} surface shows a further increase (Figure 5B). This indicates that catalysts designed for applications where water is unfavorable could employ such a combination of dopants and morphology to prevent water adsorption at the surface. For example, at a pressure of 1 bar p_{H_2O} , Y^{3+} doping reduces the desorption temperature of water by 134 K on the {111} and 35 K on the {110}. This effect increases with increasing pressure for the {111} surface but remains relatively constant for the {110} (Figure 5B). However, as dopants on the {100} surface increase the temperature of desorption compared with reduced surface, catalysts designed for applications where water is required could employ doped nanocube morphologies, i.e., those where the {100} dominates. For example, at a pressure of 1 bar, Sm^{3+} dopants increase the desorption temperature by 72 K on the {100}. This effect increases with increasing pressure (Figure 5B).

Predicted Particle Morphology. The desorption temperature corresponds to the temperature at a given partial pressure when the surface free energy of a dry surface is the same as the wet surface. We can also use these surface free energies to

predict an equilibrium morphology and, hence, infer how temperature and water partial pressure will provide a driving force for particle morphology. Using the surface energies calculated from eq 4, we can predict the relative surface area of each surface at equilibrium as a function of temperature and pressure via a Wulff construction.⁴¹ Thus, the effect of water exposure on the particle morphology can be evaluated. There are numerous ways to control the shape of CeO_2 nanoparticles and a wide variety of shapes are available, e.g., nanocubes (expressing the {100} surface) and octahedral (expressing the {111} surface and nanorods (expressing the {110} surface).⁶⁵⁻⁷³ Over time, however, this morphology may change, causing other surfaces to be expressed. Our results predict that the equilibrium particle shape as a function of temperature and pressure and, hence, suggest that there could be a thermodynamic driving force for the reconstruction of nanoparticles under conditions different from the synthesis conditions, such as those in a catalytic cycle. Our methodology provides a straightforward approach to evaluate the thermodynamic shape of nanoparticles under selected conditions and thus the final shape of the nanoparticles after being through many catalytic cycles at those conditions.

As the surface free energies depend on the number of adsorbed species, if there are more molecules on one surface simulation, at sufficiently high pressures the system with more molecules may dominate. This will only be important at high pressures but can be overcome by considering the energies of equal numbers of molecules and potentially going beyond the monolayer coverage. Figure 6 shows the result when the maximum number of water molecules on each surface is the same. Figure 6 shows the ratio between the {100}/{110} and {111} surfaces on the stoichiometric system and {100} and {111} surfaces for the reduced system in terms of area, as a function of temperature and pressure. It should be noted that on reduced and doped surfaces within this temperature and pressure range, the {110} surface is not expressed. Figure 6a shows the morphology phase diagram for the stoichiometric surface. In Figure 6a, the red region corresponds to cerium oxide octahedral nanoparticles (top left and bottom right corners). The blue region in the left side of the diagram corresponds to a truncated octahedral nanoparticle with {110} edges. On the reduced and doped surfaces there is a transition from octahedral nanoparticles at high temperature/low pressure, to truncated octahedra displaying the {100} surface at low temperature/high pressure. This effect is more pronounced on the reduced and Sm^{3+} -doped surfaces. This observation can be explained by examining the desorption temperatures for each surface. There is a large range of temperatures and pressures where the {111} surface is dry and the {100} surface is wet; thus, there is a large region where the surface energy of the {100} is being lowered by water, while the surface energy of the {111} is unchanged. We also note that at the high partial pressures and low temperatures considered there is also a prediction of increased stability of the {111} surface, although we note at these conditions that liquid water will be present and dynamics are likely to play an increasing role, which may modify the stability. It is certainly worthy of further investigation.

There are two key features from the results. First, due to the increased stability of water on the doped {100} surfaces, these surfaces will begin to be expressed (forming truncated octahedral) under more extreme conditions than for undoped reduced surface containing Ce^{3+} . For example, our results

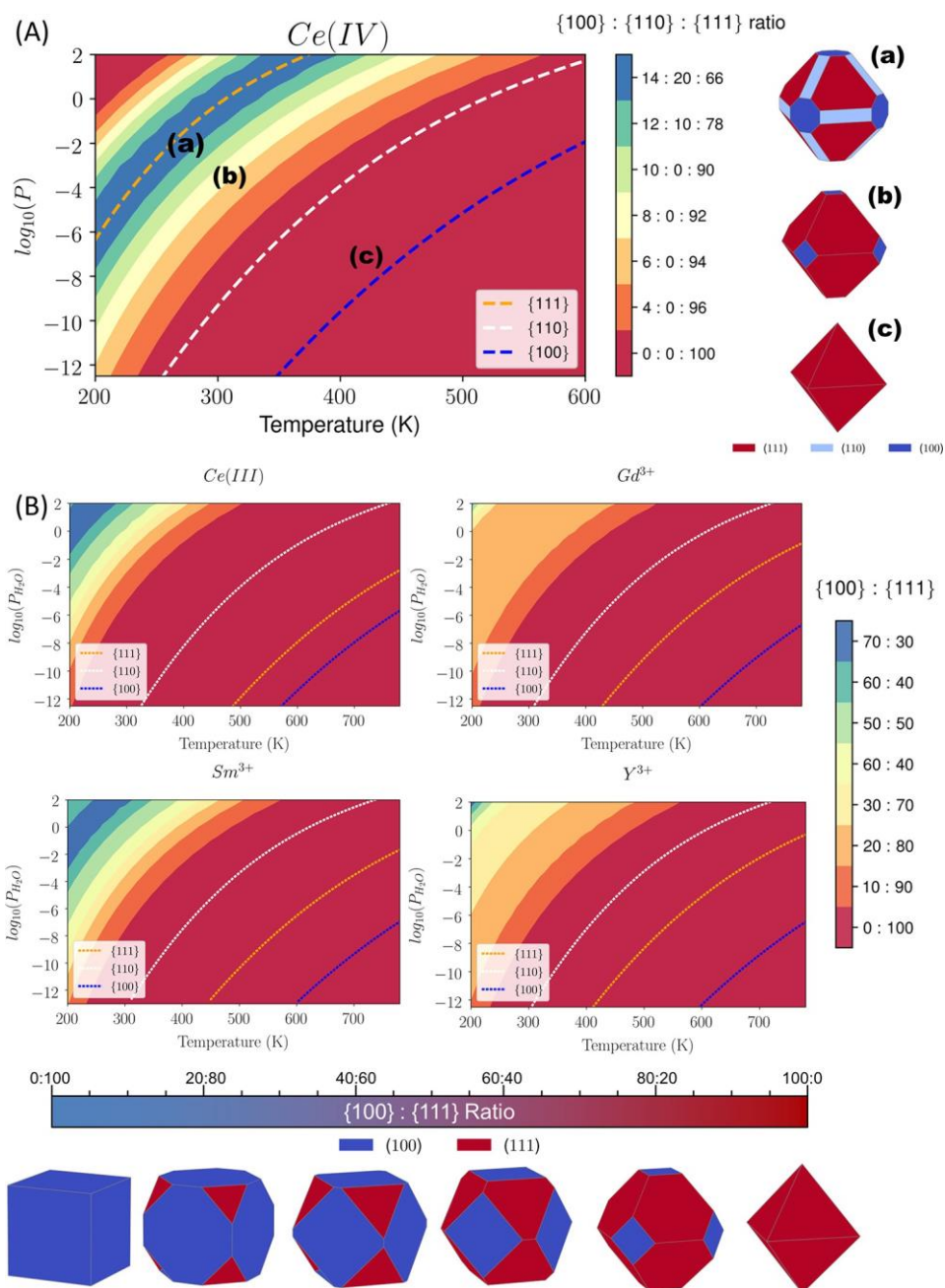


Figure 6. (A) Ratio between the {100}, {110}, and {111} surface areas as a function of temperature and pressure for the stoichiometric system. For visual clarity, nanoparticles corresponding to these ratios are shown. (B) Ratio between the {100} and {111} reduced Gd^{3+} -, Sm^{3+} -, and Y^{3+} -doped systems as a function of temperature and pressure. It should be noted that the {110} surface does not appear under these conditions for the doped systems and has thus not been included. Predicted particle morphologies across a range of surface area ratios are shown for visualization of these ratios.

suggest that doped octahedral nanoparticles, used at ultrahigh vacuum ($-10 \log_{10} P$) at 200 K, will truncate to express {100} surfaces, whereas undoped reduced (Ce^{3+} containing) surfaces will not. In contrast, nanocubes used at high temperatures will be driven toward {111} bearing octahedral nanoparticles. The change in relative stability between the {111} and {100} surfaces has been reported previously.⁷⁴

Nanoparticle Transformation. Thus far, we have considered the thermodynamics of nanoceria: from a nanocube, exposing catalytically active {100} surfaces to a nanopolyhedron with reduced exposure of active facets. However, catalysts are typically operated at high temperatures,

where the less active (polyhedral) morphology is thermodynamically more stable. It is therefore important to begin to understand the mechanism associated with the cube-to-polyhedron transformation and whether the kinetics can be controlled to preserve the material in its most active but metastable form.^{75,76}

Accordingly, we simulated the (kinetic) transformation by heating a model ceria nanocube, comprising 6921 CeO_2 repeat units and six {100} surfaces, using molecular dynamics. Snapshots of the structure of a stoichiometric and a Gd^{3+} doped nanocube are shown in Figure 7A and reveal that both nanocubes transform to a nanopolyhedra.

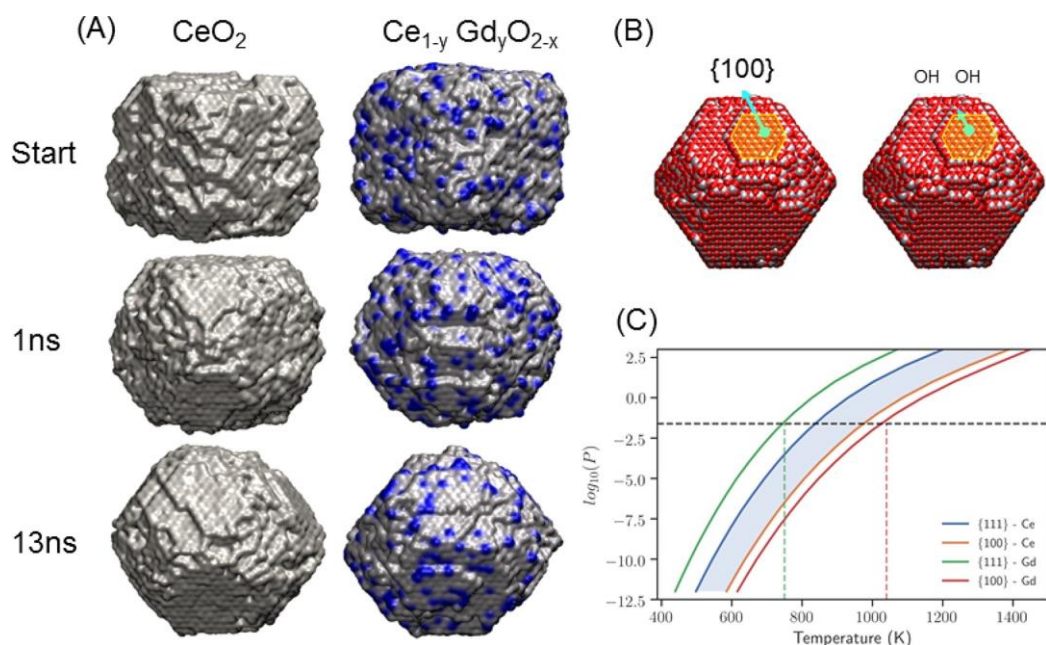


Figure 7. (A) Surface-rendered model of pure (left) and Gd^{3+} doped (right) ceria nanocubes heated to 4600 K. Start (cuboidal morphology), after 1 ns and after 13 ns (polyhedral morphology). Gd^{3+} atoms are shown as blue rendering to reveal more clearly their distribution in the nanoparticle. (B) Atoms on a $\{111\}$ surface of a ceria nanoparticle move to occupy positions on $\{100\}$ or $\{110\}$ surfaces. Water molecules block the $\{100\}$ surfaces hindering the kinetic transformation from cube to polyhedron. Water molecules are shown as schematic. Cerium is colored white, and oxygen is red. (C) Temperature of desorption of water plotted as a function of the partial pressure of water. Only the $\{111\}$ and $\{100\}$ surfaces of Ce^{3+} -reduced and Gd^{3+} -doped surfaces are presented. For example, at 1 bar, the temperature required to desorb water from a Gd^{3+} -doped $\{100\}$ surface (1130 K) is over 300 K higher than from a Gd^{3+} -doped $\{111\}$ surface (815 K).

Analysis of the nanoceria structure as it evolves over time (MD trajectories) reveals that the cube-to-polyhedron transformation is driven by the mass transport of surface ions from $\{111\}$ surfaces to $\{100\}$ surfaces, Figure 7B; the $\{111\}$ surfaces grow at the expense of $\{100\}$ surfaces. Blocking this mass transport would enable the nanoceria to exist longer in its most catalytically active (cuboidal) morphology.

Typically, capping of ceria $\{100\}$ surfaces, using, for example, oleic acid, can protect $\{100\}$ surfaces. Indeed, different capping agents can be used to selectively control the morphology of nanoceria.⁷⁷ Accordingly, we hypothesize that the presence of water, adsorbed on the $\{100\}$ surfaces, will play a similar role to capping agents in blocking mass transport to $\{100\}$ surfaces and preserving the (desirable) cuboidal morphology, Figure 7B.

Our DFT data shows that water is preferentially stabilized on the doped $\{100\}$ surfaces relative to $\{111\}$ surfaces (Figure 5 and Figure 7C). Accordingly, we predict that doping by Gd^{3+} can protect metastable (cuboidal) morphologies. In addition, experimental control over the water (partial) pressure can be used to increase the desorption energy of water on $\{100\}$ surfaces, Figure 4; the temperature required to desorb water from the $\{100\}$ increases from ~ 650 to 1025 K if the partial pressure of water is increased from 10^{-3} to 0.025 bar, Figure 4, i.e., going from vacuum to humid conditions. Accordingly, high partial pressures enable the blocking of $\{100\}$ surfaces by water at higher (operating) temperatures.

Figure 7C shows the desorption temperature for water on the $\{111\}$ and $\{100\}$ reduced and Gd^{3+} -doped surfaces. The shaded region shows the p , T conditions on the reduced surfaces where the $\{100\}$ surface (orange line) is being stabilized by water while the $\{111\}$ (blue line) is not stabilized. As dopants destabilize water on the $\{111\}$ surface and stabilize

water on the $\{100\}$ surface, dopants increase the size of this shaded region (green line/red line). Therefore, when seeking to stabilize cuboidal shaped nanoparticles there is a requirement to be aware of the relative thermodynamic stabilization of the $\{111\}$ and $\{100\}$ surfaces. Doping is clearly a way of changing the relative hydrophilicity of surfaces (i.e., this is seen as the red and green lines in Figure 7C are further apart for Gd^{3+} compared to the reduced surfaces). Water (partial) pressure could be controlled by experiment to increase water affinity for $\{100\}$ and preserve activity by retaining the structure in the cube form; i.e., mass transport would be interrupted by having water adsorbed to $\{100\}$ surfaces.

Discussion

The performance of nanoceria catalysts in the form of nanoparticles is strongly affected by the type and nature of exposed surfaces. Recent advances in the preparation of ceria nanoparticles have enabled the study of the effect of different facets on different catalytic processes.⁶⁷⁻⁷³ Here, we have shown that the particle morphology strongly affects the interaction with water, which in turn may impact upon catalytic reactions.

Ceria is used in diesel engines for the oxidation of soot,⁷⁸ which is a major air pollutant. The presence of water vapor within the exhaust mixture has been shown to negatively affect the catalyst behavior.⁷⁹ Dissociatively adsorbed water at the surfaces interferes with the NO_2 -assisted soot combustion mechanism (which exploits the high temperature induced oxidation of NO to NO_2). Surface OH groups act as adsorption sites for NO and thus hinder the catalytic oxidation of NO to NO_2 . Sm- and Y-doped ceria has been shown to have enhanced activity than its undoped counterpart for soot oxidation.⁸⁰ Soot oxidation catalysts operate between 500–900 K.⁷⁸ According to our results, water is stable on the reduced

{111}, {110}, and {100} surfaces up to a temperature of 837, 575, and 975 K at 0.025 bar, respectively; thus, on the {111} and {100} surfaces, in particular, water is present across a significant portion of the operating temperatures. Gd doping decreases the temperature range where water is stable on the {111} surface by 93 K, thus increasing the operating temperature range where water will not be present to harm the reaction. Furthermore, Y doping decreases the temperature range by a more significant margin (122 K).

The dissociation of water is an important component in the water gas shift reaction (WGSR), which is used for the oxidation of CO to CO₂ and reduction of H₂O to H₂.^{81,82} Surface selectivity toward water dissociation has been investigated and nanocubes expressing the {100} surface have been found to promote the process compared to octahedral nanoparticles expressing the {111} surface and nanorods expressing the {110} surface.^{69,83} Our results show that on reduced surfaces the dissociation of water is energetically favorable and sometimes barrierless, with this being the most favorable on the {100}. This provides an explanation for nanocubes having the highest activity for the WGSR, given that water dissociation is strongest on the {100} surface. Based upon our results, we predict that Sm doping would further improve the activity of nanocubes for the WGSR for two reasons, first, the interaction between water and the Sm doped {100} surfaces is stronger, and second, water is stable at the surface at much higher temperatures. This is not limited to the WGSR, however, and any process that requires surface water dissociation would benefit from these observations. For example, water dissociation is a key step in water splitting catalysts and in steam reforming of hydrocarbons.

Conclusions

We have shown that we can apply DFT modeling to aid in the interpretation of a number of experimental observables, via surface phase diagram evaluation, which in turn allows the prediction of nanoparticle morphology and nanoparticle evolution.

We show that by calculating reliable adsorption energies for water on different surfaces of stoichiometric and doped CeO₂, we can help in the development of a thermodynamic strategy to evaluate the nanoparticle morphology of the materials as a function of temperature and water partial pressure, two observables that can be controlled experimentally. We found that there is a driving force toward cuboidal and octahedral morphologies at low and high temperatures respectively, due to dopants reducing the affinity of water on {111} and {110} surfaces while increasing it on {100} surfaces.

Coupled with mechanistic studies using potential based MD, we predict that Gd³⁺ doping and increasing water partial pressures increase the longevity of catalytically active ceria nanocubes. The atomic-scale insights presented here quantify the interaction between the doped surfaces of CeO₂ and water, and we can begin to infer their influence on the catalytic activity. Finally, the approach outlined here can be routinely applied to any mineral surface and hence identify the temperature range where water is present and its role in defining the nanoparticle morphology.

Associated content

Supporting Information

The Supporting Information is available free of charge.

Details of first-principles calculations, Temperature vs pressure phase diagrams for all data sets, molecular dynamics study of oxygen vacancy distribution in CeO₂ nanoparticles

Author

Corresponding Authors

Adam R. Symington – *Department of Chemistry, University of Bath, Bath BA2 7AY, U.K.*; orcid.org/0000-0001-6059-497X; Email: A.R.Symington@bath.ac.uk

Stephen C. Parker – *Department of Chemistry, University of Bath, Bath BA2 7AY, U.K.*; Email: S.C.Parker@bath.ac.uk

Authors

Marco Molinari – *Department of Chemistry, University of Huddersfield, Huddersfield HD1 3DH, U.K.*; orcid.org/0000-0001-7144-6075

Samuel Moxon – *Department of Chemistry, University of Huddersfield, Huddersfield HD1 3DH, U.K.*; orcid.org/0000-0002-2972-5975

Joseph M. Flitcroft – *Department of Chemistry, University of Huddersfield, Huddersfield HD1 3DH, U.K.*; orcid.org/0000-0001-8373-0233

Dean C. Sayle – *School of Physical Science, University of Kent, Canterbury, Kent CT2 7NZ, U.K.*; orcid.org/0000-0001-7227-9010

Complete contact information is available at: <https://pubs.acs.org/10.1021/acs.jpcc.9b09046>

Author Contributions

A.R.S., M.M., S.M., J.M.F., and D.S. performed the calculations, A.R.S. analyzed the DFT data and developed the surfinpy code,⁴⁶ D.S. analyzed the MD data, S.C.P. and M.M. designed the study, and A.R.S. wrote the paper with contributions from all authors.

Notes

The authors declare no competing financial interest.

Acknowledgements

We acknowledge AWE and EPSRC (EP/P007821/1, EP/R010366/1, EP/R023603/1, EP/R513234/1, EP/M022617/1) for funding. Computations were run at the Balena HPC facility at the University of Bath, the Orion computing facility at the University of Huddersfield, and the ARCHER UK National Supercomputing Service (<http://www.archer.ac.uk>) via our membership in the UK's HEC Materials Chemistry Consortium (HEC MCC) funded by EPSRC (EP/L000202, EP/R029431); UK Materials and Molecular Modelling Hub EPSRC (EP/P020194/1).

References

- (1) Wu, J.; Tan, L. H.; Hwang, K.; Xing, H.; Wu, P.; Li, W.; Lu, Y. DNA Sequence-Dependent Morphological Evolution of Silver Nanoparticles and Their Optical and Hybridization Properties. *J. Am. Chem. Soc.* **2014**, *136*, 15195–15202.
- (2) Compton, O. C.; Osterloh, F. E. Evolution of Size and Shape in the Colloidal Crystallization of Gold Nanoparticles. *J. Am. Chem. Soc.* **2007**, *129*, 7793–7798.
- (3) Chen, P.-C.; Du, J. S.; Meckes, B.; Huang, L.; Xie, Z.; Hedrick, J. L.; Dravid, V. P.; Mirkin, C. A. Structural Evolution of Three-Component Nanoparticles in Polymer Nanoreactors. *J. Am. Chem. Soc.* **2017**, *139*, 9876–9884.

- (4) Latham, A. H.; Wilson, M. J.; Schiffer, P.; Williams, M. E. TEM-Induced Structural Evolution in Amorphous Fe Oxide Nanoparticles. *J. Am. Chem. Soc.* **2006**, *128*, 12632–12633.
- (5) Langille, M. R.; Personick, M. L.; Zhang, J.; Mirkin, C. A. Defining Rules for the Shape Evolution of Gold Nanoparticles. *J. Am. Chem. Soc.* **2012**, *134*, 14542–14554.
- (6) Jasinski, P.; Suzuki, T.; Anderson, H. U. Nanocrystalline undoped ceria oxygen sensor. *Sens. Actuators, B* **2003**, *95*, 73–77.
- (7) Elyassi, B.; Rajabbeigi, N.; Khodadadi, A.; Mohajerzadeh, S.; Sahimi, M. An yttria-doped ceria-based oxygen sensor with solid-state reference. *Sens. Actuators, B* **2004**, *103*, 178–183.
- (8) Kharton, V. V.; Figueiredo, F. M.; Navarro, L.; Naumovich, E. N.; Kovalevsky, A. V.; Yaremchenko, A. A.; Viskup, A. P.; Carneiro, A.; Marques, F. M. B.; Frade, J. R. Ceria-based materials for solid oxide fuel cells. *J. Mater. Sci.* **2001**, *36*, 1105–1117.
- (9) Kilner, J. A.; Burriel, M. Materials for Intermediate-Temperature Solid-Oxide Fuel Cells. *Annu. Rev. Mater. Res.* **2014**, *44*, 365–393.
- (10) Allen, J. P.; Gren, W.; Molinari, M.; Arrouvel, C.; Maglia, F.; Parker, S. C. Atomistic modelling of adsorption and segregation at inorganic solid interfaces. *Mol. Simul.* **2009**, *35*, 584–608.
- (11) Symington, A.; Molinari, M.; Statham, J.; Wu, J.; Parker, S. C. The role of dopant segregation on the oxygen vacancy distribution and oxygen diffusion in CeO₂ grain boundaries. *Journal of Physics: Energy* **2019**, *1*, 042005.
- (12) Yao, H.; Yao, Y. Ceria in automotive exhaust catalysts: I. Oxygen storage. *J. Catal.* **1984**, *86*, 254–265.
- (13) Chueh, W. C.; Falter, C.; Abbott, M.; Scipio, D.; Furler, P.; Haile, S. M.; Steinfeld, A. High-Flux Solar-Driven Thermochemical Dissociation of CO₂ and H₂O Using Nonstoichiometric Ceria. *Science* **2010**, *330*, 1797–1801.
- (14) Molinari, M.; Symington, A. R.; Sayle, D. C.; Sakthivel, T. S.; Seal, S.; Parker, S. C. Computer-Aided Design of Nanoceria Structures as Enzyme Mimetic Agents: The Role of Bodily Electrolytes on Maximizing Their Activity. *ACS Applied Bio Materials* **2019**, *2*, 1098–1106.
- (15) Karakoti, A. S.; Monteiro-Riviere, N. A.; Aggarwal, R.; Davis, J. P.; Narayan, R. J.; Self, W. T.; McGinnis, J.; Seal, S. Nanoceria as antioxidant: Synthesis and biomedical applications. *JOM* **2008**, *60*, 33–37.
- (16) Sakai, N.; Yamaji, K.; Horita, T.; Xiong, Y. P.; Kishimoto, H.; Yokokawa, H. Effect of Water on Oxygen Transport Properties on Electrolyte Surface in SOFCs: I. Surface Reaction Mechanism of Oxygen Isotope Exchange on Solid Oxide Electrolytes. *J. Electrochem. Soc.* **2003**, *150*, A689–A694.
- (17) Sakai, N.; Yamaji, K.; Xiong, Y. P.; Kishimoto, H.; Horita, T.; Yokokawa, H. Interaction between Water and Ceria-Zirconia-Yttria Solid Solutions. *J. Electroceram.* **2004**, *13*, 677–682.
- (18) Mogensen, M.; Jensen, K. V.; rrgensen, M. J. J.; ren Primdahl, S. Progress in understanding SOFC electrodes. *Solid State Ionics* **2002**, *150*, 123–129.
- (19) Molinari, M.; Parker, S. C.; Sayle, D. C.; Islam, M. S. Water Adsorption and Its Effect on the Stability of Low Index Stoichiometric and Reduced Surfaces of Ceria. *J. Phys. Chem. C* **2012**, *116*, 7073–7082.
- (20) Kumar, S.; Schelling, P. K. Density functional theory study of water adsorption at reduced and stoichiometric ceria(111) surfaces. *J. Chem. Phys.* **2006**, *125*, 204704.
- (21) Kumar, A.; Das, S.; Munusamy, P.; Self, W.; Baer, D. R.; Sayle, D. C.; Seal, S. Behavior of nanoceria in biologically-relevant environments. *Environ. Sci.: Nano* **2014**, *1*, 516–532.
- (22) Fronzi, M.; Piccinin, S.; Delley, B.; Traversa, E.; Stampfl, C. Water adsorption on the stoichiometric and reduced CeO₂(111) surface: a first-principles investigation. *Phys. Chem. Chem. Phys.* **2009**, *11*, 9188–9199.
- (23) Kresse, G.; Hafner, J. Ab initio molecular-dynamics simulation of the liquid-metal–amorphous-semiconductor transition in germanium. *Phys. Rev. B: Condens. Matter Mater. Phys.* **1994**, *49*, 14251–14269.
- (24) Kresse, G.; Furthmüller, J. Efficient iterative schemes for ab initio total-energy calculations using a plane-wave basis set. *Phys. Rev. B: Condens. Matter Mater. Phys.* **1996**, *54*, 11169–11186.
- (25) Dudarev, S. L.; Botton, G. A.; Savrasov, S. Y.; Humphreys, C. J.; Sutton, A. P. Electron-energy-loss spectra and the structural stability of nickel oxide: An LSDA+U study. *Phys. Rev. B: Condens. Matter Mater. Phys.* **1998**, *57*, 1505–1509.
- (26) Nolan, M.; Parker, S. C.; Watson, G. W. The electronic structure of oxygen vacancy defects at the low index surfaces of ceria. *Surf. Sci.* **2005**, *595*, 223–232.
- (27) Nolan, M.; Parker, S. C.; Watson, G. W. The electronic structure of oxygen vacancy defects at the low index surfaces of ceria. *Surf. Sci.* **2005**, *595*, 223–232.
- (28) Keating, P. R. L.; Scanlon, D. O.; Watson, G. W. Intrinsic ferromagnetism in CeO₂: dispelling the myth of vacancy site localization mediated superexchange. *J. Phys.: Condens. Matter* **2009**, *21*, 405502.
- (29) Nolan, M.; Parker, S. C.; Watson, G. W. Reduction of NO₂ on Ceria Surfaces. *J. Phys. Chem. B* **2006**, *110*, 2256–2262.
- (30) Scanlon, D. O.; Morgan, B. J.; Watson, G. W. The origin of the enhanced oxygen storage capacity of Ce_{1-x}(Pd/Pt)_xO₂. *Phys. Chem. Chem. Phys.* **2011**, *13*, 4279–4284.
- (31) Han, Z.-K.; Zhang, L.; Liu, M.; Ganduglia-Pirovano, M. V.; Gao, Y. The Structure of Oxygen Vacancies in the Near-Surface of Reduced CeO₂ (111) Under Strain. *Front. Chem.* **2019**, *7*, 436.
- (32) Zhang, C.; Michaelides, A.; King, D. A.; Jenkins, S. J. Oxygen vacancy clusters on ceria: Decisive role of cerium f electrons. *Phys. Rev. B: Condens. Matter Mater. Phys.* **2009**, *79*, No. 075433.
- (33) Campbell, C. T.; Peden, C. H. F. Oxygen Vacancies and Catalysis on Ceria Surfaces. *Science* **2005**, *309*, 713–714.
- (34) Minervini, L.; Zacate, M. O.; Grimes, R. W. Defect cluster formation in M₂O₃-doped CeO₂. *Solid State Ionics* **1999**, *116*, 339–349.
- (35) Aparicio-Angles, X.; Roldan, A.; de Leeuw, N. H. Gadolinium-Vacancy Clusters in the (111) Surface of Gadolinium-Doped Ceria: A Density Functional Theory Study. *Chem. Mater.* **2015**, *27*, 7910–7917.
- (36) Nie, L.; Mei, D.; Xiong, H.; Peng, B.; Ren, Z.; Hernandez, X. I. P.; DeLaRiva, A.; Wang, M.; Engelhard, M. H.; Kovarik, L.; Datye, A. K.; Wang, Y. Activation of surface lattice oxygen in single-atom Pt/CeO₂ for low-temperature CO oxidation. *Science* **2017**, *358*, 1419–1423.
- (37) Esch, F.; Fabris, S.; Zhou, L.; Montini, T.; Africh, C.; Fornasiero, P.; Comelli, G.; Rosei, R. Electron Localization Determines Defect Formation on Ceria Substrates. *Science* **2005**, *309*, 752–755.
- (38) Martin, P.; Spagnoli, D.; Marmier, A.; Parker, S. C.; Sayle, D. C.; Watson, G. Application of molecular dynamics DL_POLY codes to interfaces of inorganic materials. *Mol. Simul.* **2006**, *32*, 1079–1093.
- (39) Sun, Q.; Reuter, K.; Scheffler, M. Effect of a humid environment on the surface structure of RuO₂(110). *Phys. Rev. B: Condens. Matter Mater. Phys.* **2003**, *67*, 205424.
- (40) Kerisit, S.; Marmier, A.; Parker, S. C. Ab Initio Surface Phase Diagram of the 1014 Calcite Surface. *J. Phys. Chem. B* **2005**, *109*, 18211–18213.
- (41) Wulff, G. Zur Frage der Geschwindigkeit des Wachstums und der Auflösung der Krystallflächen. *Z. Kristallogr. - Cryst. Mater.* **1901**, *34*, 449.
- (42) Watson, G. W.; Kelsey, E. T.; de Leeuw, N. H.; Harris, D. J.; Parker, S. C. Atomistic simulation of dislocations, surfaces and interfaces in MgO. *J. Chem. Soc., Faraday Trans.* **1996**, *92*, 433–438.
- (43) Oliver, P. M.; Parker, S. C.; Mackrodt, W. C. Computer simulation of the crystal morphology of NiO. *Modell. Simul. Mater. Sci. Eng.* **1993**, *1*, 755–760.
- (44) Oliver, P. M.; Parker, S. C.; Mackrodt, W. C. Computer simulation of the crystal morphology of NiO. *Modell. Simul. Mater. Sci. Eng.* **1993**, *1*, 755.
- (45) Tegner, B. E.; Molinari, M.; Kerridge, A.; Parker, S. C.; Kaltsoyannis, N. Water Adsorption on AnO₂ 111, 110, and 100

Surfaces (An = U and Pu): A Density Functional Theory + U Study. *J. Phys. Chem. C* **2017**, *121*, 1675–1682.

(46) Symington, A.; Tse, J.; Molinari, M.; Marmier, A.; Parker, S. surfipy: A Surface Phase Diagram Generator. *Journal of Open Source Software* **2019**, *4*, 1210.

(47) Tran, R.; Xu, Z.; Radhakrishnan, B.; Winston, D.; Sun, W.; Persson, K. A.; Ong, S. P. Surface energies of elemental crystals. *Sci. Data* **2016**, *3*, 160080.

(48) Momma, K.; Izumi, F. VESTA3 for three-dimensional visualization of crystal, volumetric and morphology data. *J. Appl. Crystallogr.* **2011**, *44*, 1272–1276.

(49) Caddeo, F.; Corrias, A.; Sayle, D. C. Tuning the Properties of Nanoceria by Applying Force: Stress-Induced Ostwald Ripening. *J. Phys. Chem. C* **2016**, *120*, 14337–14344.

(50) Smith, W.; Forester, T. DLPOLY2.0: A general-purpose parallel molecular dynamics simulation package. *J. Mol. Graphics* **1996**, *14*, 136–141.

(51) Morgan, L. M.; Molinari, M.; Corrias, A.; Sayle, D. C. Protecting Ceria Nanocatalysts-The Role of Sacrificial Barriers. *ACS Appl. Mater. Interfaces* **2018**, *10*, 32510–32515.

(52) Bhatta, U. M.; Reid, D.; Sakthivel, T.; Sayle, T. X. T.; Sayle, D.; Molinari, M.; Parker, S. C.; Ross, I. M.; Seal, S.; Mbus, G. Morphology and Surface Analysis of Pure and Doped Cuboidal Ceria Nanoparticles. *J. Phys. Chem. C* **2013**, *117*, 24561–24569.

(53) Sayle, T. X. T.; Molinari, M.; Das, S.; Bhatta, U. M.; Mbus, G.; Parker, S. C.; Seal, S.; Sayle, D. C. Environment-mediated structure, surface redox activity and reactivity of ceria nanoparticles. *Nanoscale* **2013**, *5*, 6063–6073.

(54) Sayle, T. X. T.; Cantoni, M.; Bhatta, U. M.; Parker, S. C.; Hall, S. R.; Mbus, G.; Molinari, M.; Reid, D.; Seal, S.; Sayle, D. C. Strain and Architecture-Tuned Reactivity in Ceria Nanostructures; Enhanced Catalytic Oxidation of CO to CO₂. *Chem. Mater.* **2012**, *24*, 1811–1821.

(55) Sayle, T. X. T.; Inkson, B. J.; Karakoti, A.; Kumar, A.; Molinari, M.; Mbus, G.; Parker, S. C.; Seal, S.; Sayle, D. C. Mechanical properties of ceria nanorods and nanochains; the effect of dislocations, grain-boundaries and oriented attachment. *Nanoscale* **2011**, *3*, 1823–1837.

(56) Minervini, L.; Zacate, M. O.; Grimes, R. W. Defect cluster formation in M₂O₃-doped CeO₂. *Solid State Ionics* **1999**, *116*, 339–349.

(57) Humphrey, W.; Dalke, A.; Schulten, K. VMD: Visual molecular dynamics. *J. Mol. Graphics* **1996**, *14*, 33–38.

(58) Skorodumova, N. V.; Baudin, M.; Hermansson, K. Surface properties of CeO₂ from first principles. *Phys. Rev. B: Condens. Matter Mater. Phys.* **2004**, *69*, No. 075401.

(59) Jeyaranjan, A.; Sakthivel, T. S.; Molinari, M.; Sayle, D. C.; Seal, S. Morphology and Crystal Planes Effects on Supercapacitance of CeO₂ Nanostructures: Electrochemical and Molecular Dynamics Studies. *Particle & Particle Systems Characterization* **2018**, *35*, 1800176.

(60) Mullins, D. R.; Albrecht, P. M.; Chen, T.-L.; Calaza, F. C.; Biegalski, M. D.; Christen, H. M.; Overbury, S. H. Water Dissociation on CeO₂(100) and CeO₂(111) Thin Films. *J. Phys. Chem. C* **2012**, *116*, 19419–19428.

(61) Watkins, M. B.; Foster, A. S.; Shluger, A. L. Hydrogen Cycle on CeO₂ (111) Surfaces: A Density Functional Theory Calculations. *J. Phys. Chem. C* **2007**, *111*, 15337–15341.

(62) Perez-Coll, D.; Mather, G. C. Electrical transport at low temperatures in dense nanocrystalline Gd-doped ceria. *Solid State Ionics* **2010**, *181*, 20–26.

(63) Kossov, A.; Cohen, H.; Bendikov, T.; Wachtel, E.; Lubomirsky, I. Water adsorption at the surface of pure and Gd-doped ceria. *Solid State Ionics* **2011**, *194*, 1–4.

(64) Chen, B.; Ma, Y.; Ding, L.; Xu, L.; Wu, Z.; Yuan, Q.; Huang, W. Reactivity of Hydroxyls and Water on a CeO₂(111) Thin Film Surface: The Role of Oxygen Vacancy. *J. Phys. Chem. C* **2013**, *117*, 5800–5810.

(65) Trovarelli, A.; Llorca, J. Ceria Catalysts at Nanoscale: How Do Crystal Shapes Shape Catalysis? *ACS Catal.* **2017**, *7*, 4716–4735.

(66) McDowell, M. T.; Lichterman, M. F.; Carim, A. I.; Liu, R.; Hu, S.; Brunschwig, B. S.; Lewis, N. S. The Influence of Structure and Processing on the Behavior of TiO₂ Protective Layers for Stabilization of n-Si/TiO₂/Ni Photoanodes for Water Oxidation. *ACS Appl. Mater. Interfaces* **2015**, *7*, 15189–15199.

(67) Florea, I.; Feral-Martin, C.; Majimel, J.; Ihiawakrim, D.; Hirlimann, C.; Ersen, O. Three-Dimensional Tomographic Analyses of CeO₂ Nanoparticles. *Cryst. Growth Des.* **2013**, *13*, 1110–1121.

(68) Si, R.; Flytzani-Stephanopoulos, M. Shape and Crystal-Plane Effects of Nanoscale Ceria on the Activity of Au-CeO₂ Catalysts for the Water Gas Shift Reaction. *Angew. Chem., Int. Ed.* **2008**, *47*, 2884–2887.

(69) Mai, H.-X.; Sun, L.-D.; Zhang, Y.-W.; Si, R.; Feng, W.; Zhang, H.-P.; Liu, H.-C.; Yan, C.-H. Shape-Selective Synthesis and Oxygen Storage Behavior of Ceria Nanopolyhedra, Nanorods, and Nanocubes. *J. Phys. Chem. B* **2005**, *109*, 24380–24385.

(70) Asahina, S.; Takami, S.; Otsuka, T.; Adschiri, T.; Terasaki, O. Exploitation of Surface-Sensitive Electrons in Scanning Electron Microscopy Reveals the Formation Mechanism of New Cubic and Truncated Octahedral CeO₂ Nanoparticles. *ChemCatChem* **2011**, *3*, 1038–1044.

(71) Yang, C.; Yu, X.; Heiyaler, S.; Nefedov, A.; Colussi, S.; Llorca, J.; Trovarelli, A.; Wang, Y.; Wall, C. Surface Faceting and Reconstruction of Ceria Nanoparticles. *Angew. Chem., Int. Ed.* **2017**, *56*, 375–379.

(72) Crozier, P. A.; Wang, R.; Sharma, R. In situ environmental TEM studies of dynamic changes in cerium-based oxides nanoparticles during redox processes. *Ultramicroscopy* **2008**, *108*, 1432–1440.

(73) Lin, Y.; Wu, Z.; Wen, J.; Poeppelmeier, K. R.; Marks, L. D. Imaging the Atomic Surface Structures of CeO₂ Nanoparticles. *Nano Lett.* **2014**, *14*, 191–196.

(74) Kropp, T.; Paier, J.; Sauer, J. Interactions of Water with the (111) and (100) Surfaces of Ceria. *J. Phys. Chem. C* **2017**, *121*, 21571–21578.

(75) Castanet, U.; Feral-Martin, C.; Demourgues, A.; Neale, R. L.; Sayle, D. C.; Caddeo, F.; Flitcroft, J. M.; Caygill, R.; Pointon, B. J.; Molinari, M.; Majimel, J. Controlling the 111/110 Surface Ratio of Cuboidal Ceria Nanoparticles. *ACS Appl. Mater. Interfaces* **2019**, *11*, 11384–11390.

(76) Asghar, M. S. A.; Inkson, B.; Seal, S.; Molinari, M.; Sayle, D.; Mbus, G. In-situ observation of radiation physics and chemistry of nanostructured cerium oxide in water. *Mater. Res. Express* **2019**, *6*, No. 015032.

(77) Raza Naqvi, S. T.; Shirinfar, B.; Majeed, S.; Najam-ul Haq, M.; Hussain, D.; Iqbal, T.; Ahmed, N. Synthesis, design and sensing applications of nanostructured ceria-based materials. *Analyst* **2018**, *143*, 5610–5628.

(78) LIU, S.; WU, X.; WENG, D.; RAN, R. Ceria-based catalysts for soot oxidation: a review. *J. Rare Earths* **2015**, *33*, 567–590.

(79) Hernandez-Gimenez, A. M.; Lozano-Castello, D.; Bueno-Lopez, A. Effect of CO₂, H₂O and SO₂ in the ceria-catalyzed combustion of soot under simulated diesel exhaust conditions. *Appl. Catal., B* **2014**, *148–149*, 406–414.

(80) Krishna, K.; Bueno-Lopez, A.; Makkee, M.; Moulijn, J. Potential rare earth modified CeO₂ catalysts for soot oxidation: I. Characterisation and catalytic activity with O₂. *Appl. Catal., B* **2007**, *75*, 189–200.

(81) Pal, D.; Chand, R.; Upadhyay, S.; Mishra, P. Performance of water gas shift reaction catalysts: A review. *Renewable Sustainable Energy Rev.* **2018**, *93*, 549–565.

(82) Trimm, D. Minimisation of carbon monoxide in a hydrogen stream for fuel cell application. *Appl. Catal., A* **2005**, *296*, 1–11.

(83) Wu, Z.; Li, M.; Overbury, S. H. On the structure dependence of CO oxidation over CeO₂ nanocrystals with well-defined surface planes. *J. Catal.* **2012**, *285*, 61–73.